

1

# Physics-dynamics coupling with element-based high-order Galerkin 2 methods: quasi equal-area physics grid

3 Adam R. Herrington\*

4 *School of Marine and Atmospheric Sciences, Stony Brook University, Stony Brook, New York,  
5 USA.*

6 Peter H. Lauritzen

7 *Climate and Global Dynamics, National Center for Atmospheric Research, 1850 Table Mesa  
8 Drive, Boulder, Colorado, USA.*

9 Mark A. Taylor

10 *Sandia National Laboratories, Albuquerque, New Mexico, USA.*

11 Steve Goldhaber and Brian E. Eaton

12 *Climate and Global Dynamics, National Center for Atmospheric Research, 1850 Table Mesa  
13 Drive, Boulder, Colorado, USA.*

14 Kevin A. Reed

15 *School of Marine and Atmospheric Sciences, Stony Brook University, State University of New  
16 York, Stony Brook, New York.*

17 Paul A. Ullrich

<sup>18</sup> Department of Land, Air and Water Resources, University of California, Davis, California, USA.

<sup>19</sup> \*Corresponding author address: Adam R. Herrington, School of Marine and Atmospheric Sciences, Stony Brook University, Stony Brook, New York, USA.

<sup>20</sup> E-mail: adam.herrington@stonybrook.edu

## ABSTRACT

Atmospheric modeling with element-based high-order Galerkin methods presents a unique challenge to the conventional physics-dynamics coupling paradigm, due to the highly irregular distribution of nodes within an element and the distinct numerical characteristics of the Galerkin method. The conventional coupling procedure is to evaluate the physical parameterizations (*physics*) on the dynamical core grid. Evaluating the physics at the nodal points exacerbates numerical noise from the Galerkin method, enabling and amplifying local extrema at element boundaries. Grid imprinting may be substantially reduced through the introduction of an entirely separate, approximately isotropic finite-volume grid for evaluating the physics forcing. Integration of the spectral basis over the control-volumes provides an area average state to the physics, which is more representative of the state in the vicinity of the nodal points rather than the nodal point itself, and is more consistent with the notion of a ‘large-scale state’ required by conventional physics packages.

This study documents the implementation of a quasi-equal area physics grid into NCAR’s Community Atmosphere Model with Spectral Elements, and is shown to be effective at mitigating grid imprinting in the solution. The physics grid is also appropriate for coupling to other components within the Community Earth System Model, since the coupler requires component fluxes to be defined on a finite-volume grid, and one can be certain that the fluxes on the physics grid are indeed, volume-averaged.

43 **1. Introduction**

44 An increasing number of numerical methods publications in the atmospheric science literature  
45 concern transport, shallow-water, and three-dimensional models employing element-based high-  
46 order Galerkin discretizations such as finite-element and discontinuous Galerkin methods (for an  
47 introduction to these methods see, e.g., Durran 2010; Nair et al. 2011; Ullrich 2014). Some global  
48 models based on Galerkin methods have reached a level of maturity for which they are being con-  
49 sidered for next generation climate and weather models due to their inherent conservation proper-  
50 ties, high-order accuracy (for smooth problems), high parallel efficiency, high processor efficiency,  
51 and geometric flexibility facilitating mesh-refinement applications. NCAR’s Community Atmo-  
52 sphere Model (CAM; Neale et al. 2012) offers a dynamical core based on continuous Galerkin  
53 finite elements (Taylor and Fournier 2010), referred to as CAM-SE (CAM Spectral Elements;  
54 Taylor et al. 2008; Dennis et al. 2012; Lauritzen et al. 2018). CAM-SE is, in particular, being used  
55 for high resolution climate modeling (e.g., Small et al. 2014; Reed et al. 2015; Bacmeister et al.  
56 2018) and static mesh-refinement applications (e.g., Fournier et al. 2004; Zarzycki et al. 2014a,b;  
57 Guba et al. 2014b; Rhoades et al. 2016). Other examples of models based on high-order Galerkin  
58 methods that are being considered for ‘operational’ weather-climate applications are Giraldo and  
59 Restelli (2008), Nair et al. (2009), Brdar et al. (2013) and E3SM (<https://e3sm.org/>).

60 Assumptions inherent to the physical parameterizations (also referred to as *physics*) require  
61 the state passed by the dynamical core represent a ‘large-scale state’, for example, in quasi-  
62 equilibrium-type convection schemes (Arakawa and Schubert 1974; Plant 2008). In finite-volume  
63 methods (e.g., Lin 2004), one may think of the dynamical core state as the average state of the  
64 atmosphere over a control volume, and for resolutions typical of climate simulations is entirely  
65 consistent with the notion of a ‘large-scale state’. For finite-difference methods (e.g., Suarez et al.

66 1983) the point value is thought of as representative for the atmospheric state in the vicinity of the  
67 point value and one can usually associate a volume with the grid-point. Hence the physics grid (the  
68 grid on which the state of the atmosphere is evaluated and passed to physics) and the dynamics  
69 grid (the grid the dynamical core uses) coincide. Having the physics and dynamics grids coin-  
70 cide is obviously convenient since no interpolation is needed (which could disrupt conservation  
71 properties) and the number of degrees of freedom on both grids is exactly the same.

72 For the regular latitude-longitude, cubed-sphere and icosahedral grids the distance between the  
73 grid-points is gradually varying for finite-volume/finite-difference discretizations. Examples of  
74 models that use these grids are CAM-FV (latitude-longitude grid, Lin 2004), FV3 (cubed-sphere  
75 grid, Putman and Lin 2007) and ICON (icosahedral grid, Wan et al. 2013). For high-order  
76 element-based Galerkin methods, the dynamical core grid is defined by the quadrature points. In  
77 CAM-SE, these are the Gauss-Lobatto-Legendre (GLL) quadrature nodes. A unique aspect of the  
78 high-order quadrature rules is that the nodes within an element are located at the roots of the basis  
79 set, which may be irregularly spaced. For example, Figure 1 shows GLL points on an individual  
80 element of a cubed-sphere grid for degree 3 ( $np \times np = 4 \times 4$  quadrature points) and degree 7  
81 ( $np \times np = 8 \times 8$  quadrature points) Lagrange polynomial basis used in CAM-SE. The higher  
82 the order of the quadrature rule, the greater variance in distance between GLL quadrature points  
83 within an element. GLL quadrature points cluster near the edges and, in particular, the corners of  
84 the elements.

85 The resolved scales of motion are not determined by the distance between quadrature nodes,  
86 but rather the degree of the polynomial basis in each element. The nodes may be viewed as  
87 irregularly spaced samples of an underlying spectrally truncated state. From this perspective, one  
88 might expect the nodal solutions to be independent of location within an element. While the  
89 interior quadrature nodes are  $C^\infty$  in CAM-SE (i.e. the basis representation is infinitely smooth

and all derivatives are continuous), the smoothness of boundary nodes are constrained by the need to patch neighboring solutions together to form the global basis set, an operation known as the direct stiffness summation (DSS; Maday and Patera 1987; Canuto et al. 2007). The DSS operation is attractive because it allows for high-order accuracy with minimal communication between elements, but degrades the solution to  $C^0$  at element boundaries (i.e., all derivatives are discontinuous). Through evaluating the physics at the nodal points, strong grid-scale forcing or oscillatory behavior near an element boundary may exacerbate the discontinuity, and our initial expectation, that the nodal solutions are independent of within-element location, is unlikely for non-smooth problems, e.g., the presence of rough topography or moist physics grid-scale forcing.

It is the purpose of this paper to document the implementation of an entirely separate, quasi-equal area finite-volume physics grid into CAM-SE. In this framework, the dynamical core state is integrated over control volumes to provide a volume averaged state to the physics, thereby minimizing the influence of any one particular nodal value on the physics forcing. Section 2 provides a thorough explanation of how grid imprinting manifests in high-order Galerkin methods for non-smooth problems. The implementation of the physics grid configuration into CAM-SE is presented in Section 3. Results from a hierarchy of idealized model configurations are presented in Section 4, illustrating the physics grid is effective at mitigating undesirable grid imprinting in the solution. Section 5 contains a discussion of results and concluding remarks.

## 2. The Quadrature Node Problem

Figure 2 is a schematic illustrating in one-dimension how grid-imprinting is enabled by the physics, when the dynamical core is built with high-order Galerkin methods. The schematic depicts a time-step, starting from smooth initial conditions (Figure 2a), and subsequently advancing the dynamics one Runge-Kutta time-step (Figure 2b). Since the boundary nodes of adjacent el-

ements overlap one-another, there are now two solutions for each boundary node. The DSS operator, effectively a numerical flux applied to the element boundaries such that overlapping nodal values agree, is applied (Figure 2c), degrading the boundary nodes to  $C^0$  in the process. This discontinuity may be exacerbated if, e.g., the physics updates the state at an element boundary (Figure 2d,e), resulting in characteristically tighter gradients on the boundary nodes compared to if the physics forcing were applied to an interior node (Figure 2g,h).

To test the degree to which nodal solutions depend on within-element position, an aqua-planet simulation (Neale and Hoskins 2000; Medeiros et al. 2016), which consists of an ocean covered planet in perpetual equinox, with fixed, zonally symmetric sea surface temperatures idealized after the present day climatology, is carried out using CAM-SE, using CAM, version 4 physics (CAM4; Neale et al. 2010) and run for one year. The nominal low resolution *ne30np4* grid is used, pertaining to an average equatorial grid spacing of 111.2km. The probability density distribution of the upward vertical pressure velocity ( $\omega$ ), conditionally sampled based on three categories - ‘interior’, ‘edge’ and ‘corner’ nodes - is provided in Figure 3a. The rationale for concentrating on the  $\omega$  field is that it closely follows divergent modes, which are sensitive to the discontinuous pressure gradients that characterize boundary nodes. There is an apparent dependence on nodal location, with interior nodes being characteristically sluggish, and corner and edge nodes having systematically larger magnitude vertical motion. This behavior is consistent with the smoothness properties of the different nodal locations, with discontinuous pressure gradients resulting in greater vertical motion at edge and corner nodes. The main division of solutions shown in Figure 3a is primarily between whether a node is, or is not situated on an element boundary, and is a nuanced signature of high-order element-based Galerkin methods for non-smooth problems.

If the conventional physics-dynamics coupling paradigm is applied to CAM-SE, then the physics are to be evaluated at the GLL nodes, and a volume associated with the quadrature point should

be defined. One approach to construct this grid is to decompose each spectral element into  $(np - 1) \times (np - 1)$  subcells and then take the dual grid of this subcell grid. For cubed-sphere meshes, this dual grid will have a control volume associated with each quadrature point. These control volumes will be triangles for the cube corner quadrature points and quadrilaterals for all remaining quadrature points. Newton iteration can then be used to adjust the corners of these control volumes so that their spherical area exactly match the Gaussian weight multiplied by the metric term (these weights are used for integrating the basis functions over the elements and can therefore, in this context, be interpreted as areas). For cubed-sphere meshes, the Newton iteration can be replaced by a direct method if some of the quadrilaterals are replaced by pentagons giving additional flexibility in matching the spherical area to the quadrature weights. Such a dual grid is shown in Figure 4. This grid is used in the NCAR CESM (Community Earth System Model) coupler for passing states between ocean, atmosphere and land components since the current remapping method is finite-volume based and therefore requires control volumes (it is noted that methods exist that do not require control volumes for conservative interpolation, e.g., Ullrich and Taylor (2015)). Hence the components ‘see’ an irregular atmospheric grid. Similarly, the parameterizations in the atmosphere ‘see’ a state that is anisotropically sampled in space (see Figure 1 and 5 in Kim et al. 2008).

The quadrature grid in element-based Galerkin methods is defined to perform mathematical operations on the basis functions, e.g., computing gradients and integrals, rather than evaluating the state variables for physics-dynamics coupling. One may argue that it would be more consistent to integrate the basis functions over quasi-equal area control volumes within each element and pass those control volume average values to physics rather than irregularly spaced quadrature point values. In this case when integrating basis functions over control volumes a grid-cell average value is more representative of the values near the extrema at the element boundary than the quadrature

161 point value. The relationship between the nodal values, the basis functions and the proposed  
162 control volumes is illustrated schematically in one-dimension in parts (f) and (i) in Figure 2.

163 **3. Methods**

164 Here we focus on CAM-SE, however, in principle the methods apply to any element-based high-  
165 order Galerkin model. The physics grid in CAM-SE is defined by sub-dividing each element using  
166 equi-angular gnomonic coordinate lines to define the sides of the physics grid control volumes (see  
167 the Appendix for details). Note that the element boundaries are defined by equi-angular gnomonic  
168 grid lines. The notation  $pg = 3$  refers to the configuration where the elements are divided into  
169  $pg \times pg = 3 \times 3$  equi-angular physics grid cells (see Figure 5) **resulting in a quasi-equal spherical**  
170 **area grid**. Defining the physics grid by sub-dividing elements makes it possible to use the same el-  
171 ement infrastructure as already used in CAM-SE, thereby facilitating its implementation. Here we  
172 make use of the *ne30np4* and *ne30pg3* grids that use GLL quadrature point physics grid (physics  
173 and dynamics grid coincide), and the same ( $pg = 3$ ) resolution quasi equal-area physics grids, re-  
174 spectively. In all configurations we use degree three Lagrange basis ( $np = 4$ ) and  $ne \times ne = 30 \times 30$   
175 elements on each cubed-sphere panel.

176 A consequence of separating physics and dynamics grids is that the atmospheric state must be  
177 mapped to the physics grid and the physics tendencies must be mapped back to the dynamics  
178 grid. This is discussed in separate sections below. When separating physics and dynamics grids it  
179 is advantageous to use a vertical coordinate that is static during physics-dynamics coupling. This  
180 was one motivation to switch to a dry-mass vertical coordinate in CAM-SE (Lauritzen et al. 2018);  
181 since dry mass remains constant throughout physics the dry-mass vertical coordinate remains fixed  
182 during physics-dynamics coupling. **The dry mass coordinate subsequently evolves as floating**  
183 **Lagrangian layers by the dynamics (Lin 2004) periodically mapped back to a reference hybrid-**

184 sigma-pressure coordinate after Simmons and Burridge (1981). All variables mapped between  
185 grids are collocated, layer-mean values (Lauritzen et al. 2018).

186 *a. Mapping state from dynamics grid (GLL) to physics grid (pg)*

187 The dynamics state is defined on the GLL grid in terms of temperature  $T^{(gll)}$ , zonal wind com-  
188 ponent  $u^{(gll)}$ , meridional wind component  $v^{(gll)}$ , and dry pressure level thickness  $\Delta p^{(gll)}$ . In the  
189 mapping of the atmospheric state to the physics grid it is important that the following properties  
190 are met:

- 191 1. conservation of scalar quantities such as mass and dry thermal energy,
- 192 2. for tracers; shape-preservation (monotonicity), i.e. the mapping method must not introduce  
193 new extrema in the interpolated field, in particular, negatives,
- 194 3. consistency, i.e. the mapping preserves a constant,
- 195 4. linear correlation preservation.

196 Other properties that may be important, but not pursued here, includes total energy conservation  
197 and axial angular momentum conservation; the main reason being that we did not manage to  
198 construct a high-order reversible map that is consistent, shape-preserving and conservative. Also,  
199 enforcing total energy conservation locally using, e.g. Lin (2004)'s method where total energy and  
200 velocity components are remapped and temperature is a derived variable, has proven problematic  
201 (C. Chen, personal communication).

202 We argue that the most consistent method for mapping scalar state variables from the GLL grid  
203 to the physics grid is to integrate the Lagrange basis function representation (used by the SE dy-  
204 namical core) over the physics grid control volumes, i.e. integrate the basis function representation  
205 of  $\Delta p^{(gll)} \times T^{(gll)}$  and  $\Delta p^{(gll)}$  over the physics grid control volume (see, e.g., Lauritzen et al. 2017;

$$\Delta p^{(pg)} = \frac{1}{A^{(pg)}} \int_{A^{(pg)}} \Delta p^{(gll)} dA, \quad (1)$$

$$T^{(pg)} = \frac{1}{A^{(pg)} \Delta p^{(pg)}} \int_{A^{(pg)}} T^{(gll)} \Delta p^{(gll)} dA, \quad (2)$$

207 where  $A^{(pg)}$  is the physics grid area. The integrals are numerically computed using the GLL  
 208 quadrature rule which exactly (to machine precision) integrates the basis functions over the  $pg$   
 209 control volumes (Lauritzen et al. 2017). Thermal energy and dry air mass is conserved and the  
 210 mapping is consistent. For the wind, which is a vector, the zonal and meridional wind components  
 211 are mapped by transforming to contra-variant wind components, evaluating the basis function  
 212 representation thereof at the equi-angular center of the physics grid control volumes and then  
 213 transformed back to latitude-longitude coordinate system winds. All of the operations are local to  
 214 the element and do not require communication between elements.

215 The mapping of tracers is more problematic since the SE basis function representation is oscil-  
 216 latory although the shape-preserving filter guarantees shape-preservation at the GLL nodes (Guba  
 217 et al. 2014a). To avoid this issue we use the CAM-SE-CSLAM version of CAM-SE (Conservative  
 218 Semi-Lagrangian Multi-tracer transport scheme Lauritzen et al. 2017), where tracers are advected  
 219 on the  $pg = 3$  physics grid. Note that in CAM-SE-CSLAM the dry mass internally predicted by  
 220 CSLAM,  $\Delta p^{(cslam)}$ , is, by design, equal to  $\Delta p^{(gll)}$  integrated over the CSLAM/physics grid con-  
 221 trol volume (Lauritzen et al. 2017). Since the tracer grid and physics grids are co-located and  
 222  $\Delta p^{(pg)} = \Delta p^{(cslam)}$  then the mass conservation, correlation preservation, consistency and shape-  
 223 preservation constraints are inherently fulfilled.

224 b. *Mapping tendencies from physics grid (pg) to dynamics grid (GLL)*

225 The physics tendencies are computed on the finite-volume physics grid and are denoted  
226  $f_T^{(pg)}, f_u^{(pg)}, f_v^{(pg)}$ , and  $f_m^{(pg)}$ . Note that dry air mass is not modified by physics and hence there  
227 is no tendency for dry mass,  $f_{\Delta p} \equiv 0$ . Also, it is important to map tendencies and not state from  
228 the physics grid to GLL grid otherwise one will get spurious tendencies from mapping errors when  
229 the actual physics tendency is zero (unless a reversible map is used).

230 It is important that this process:

231 1. for tracers; mass tendency is conserved,

232 2. for tracers; in each tracer grid cell the mass tendency from physics must not exceed tracer  
233 mass available in tracer grid cell (it is assumed that the physics tendency will not drive tracer  
234 mixing ratio negative on the physics grid),

235 3. linear correlation preservation,

236 4. consistency, i.e. the mapping preserves a constant tendency.

237 Other properties that may be important, but not pursued here, includes total energy conservation  
238 (incl. components of total energy) and axial angular momentum conservation. Scalar variables  
239 are mapped from **the** physics grid to GLL grid using a tensor-product Lagrange interpolation **in**  
240 **two dimensions (i.e. we assume that the pressure variations in the vertical are small)**. The local  
241 coordinates on a cubed-sphere are discontinuous at the element edges so the interpolation requires  
242 special attention at the cube corners and edges. The details are provided in the Appendix. Lagrange  
243 interpolation preserves a constant (including zero) and linear correlations. Tracer and physics grids  
244 are co-located so tracer mass, tracer shape, and tracer correlations are trivially preserved on the  
245 tracer grid; and the inconsistency in point 2 above will not appear.

246 Mapping from  $pg$  to  $GLL$  grids while conserving mass was found to be difficult without ex-  
247 cessive grid imprinting at element edges. Mass-conservation (using conventional finite-volume  
248 methods) requires a control volume to be defined around the  $GLL$  points (see, .e.g., Figure 4 in  
249 this paper or Figure 8b in Ullrich et al. 2016). These volumes are artificial and not consistent with  
250 the SE method. Integrating the CSLAM reconstruction of water tracers of such artificial control  
251 volumes led to  $GLL$  node grid imprinting in the mapping and will not preserve a constant mixing  
252 ratio since the mapping of  $\Delta p^{(pg)}$  to  $GLL$  will not yield the  $GLL$  node value for dry pressure-level  
253 thickness (i.e. the maps are not reversible).

254 It was also found important to use an interpolator that is smooth across element boundaries.  
255 Using an algorithm that only uses information from an element of control volumes will (at best)  
256 be  $C^0$  at the element boundaries and therefore lead to boundary node grid imprinting. A stencil  
257 that extends beyond one element is therefore necessary. After much experimentation, the best  
258 results in terms of grid-imprinting were obtained with tensor-cubic interpolation and by using the  
259 CAM-SE-CSLAM configuration (which requires the same boundary exchange/communication as  
260 used in CSLAM).

261 *c. Time splitting and physics-dynamics coupling*

262 The physics and dynamics are integrated in time using a sequential-update approach (e.g.,  
263 Williamson 2002). The dynamical core is sub-cycled over the (usually) longer physics time-step,  
264  $\Delta t_{phys}$ , e.g., the vertical remapping time-step  $\Delta t_{remap}$  is cycled  $rsplit$  times, summing to  $\Delta t_{phys}$ . In  
265 CAM-SE, a fraction of the physics forcing, e.g.,  $f_q \times \Delta t_{remap}$  is applied at the beginning of each  
266  $rsplit$  vertical remap subcycles, such that the full forcing ( $f_q \times \Delta t_{phys}$ ) is realized over the course  
267 of a physics time-step. This approach of dribbling the tendencies over sub-intervals has the ad-  
268 vantage of reducing gravity wave noise (Thatcher and Jablonowski 2016), but may disrupt tracer

269 mass conservation (Zhang et al. 2017). In CAM-SE-CSLAM, all but the tracer mass quantities are  
270 dribbled, with tracer mass receiving the full physics update, e.g.,  $f_q \times \Delta t_{phys}$ , applied only at the  
271 beginning of the first remap sub-cycle, and thereby conserving tracer mass. This is the  $f_{type} = 2$   
272 configuration described in detail in Section 3.6.3 in Lauritzen et al. (2018).

273 In the SE integration of the equations of motion on the GLL grid the water species are  
274 needed in the computation of the pressure gradient force and generalized expressions for heat  
275 capacity at constant pressure  $c_p$ , etc. Hence the mixing ratios for water vapor and dynamical-  
276 thermodynamically active condensates (e.g., cloud ice, cloud liquid, ...) are needed on the  
277 GLL grid. We have chosen to advect the water species on the GLL grid using the SE method as  
278 well as on the physics grid using CSLAM. Every time physics updates the water species on the  
279 CSLAM grid, a forcing term (equal to the difference between updated CSLAM water variables and  
280 the SE values) is applied to the GLL water variables using dribbling so that the CSLAM solution  
281 and SE solution for water species are tightly coupled.

## 282 4. Results

283 A hierarchy of idealized model configurations are presented in order to elucidate the differ-  
284 ences between CAM-SE and CAM-SE-CSLAM (available from the CESM2.1 release; <https://doi.org/10.5065/D67H1H0V>). Here, the configurations are presented in order of increas-  
285 ing complexity, each with a pair of approximately  $1^\circ$  simulations, pertaining to the *ne30np4* and  
286 *ne30pg3* grids, and a  $\Delta t_{phys} = 1800$  s.  
287

### 288 a. *Moist Baroclinic Wave*

289 The moist baroclinic wave test case was developed as part of the ‘CESM Simple Models’ project  
290 (Polvani et al. 2017), and included in the release of CESM2. It is effectively the dry test-case of

291 Ullrich et al. (2014), but initialized with moisture and coupled to the Kessler moist physics routine  
292 (Kessler 1969). For more details on this test case (which was part of the 2016 Dynamical Core  
293 Model Intercomparison Project, see Ullrich et al. 2017), see Section 4.1 in Lauritzen et al. (2018).  
294 A measure of the uncertainty of the reference solution, the  $L_2$  difference norm between two high-  
295 resolution solutions using different dynamical cores, was also presented in Lauritzen et al. (2018)  
296 and provided again here in Figure 6. The  $L_2$  norm between CAM-SE and CAM-SE-CSLAM lies  
297 below the uncertainty of the reference solution, indicating their differences are insignificant.

298 The flow field of the baroclinic wave test is used to drive the terminator "toy"-chemistry test  
299 of Lauritzen et al. (2015b). The terminator test is used to assess the tracer mass conservation  
300 properties for linear-correlated reactive species being advected across the terminator line. The  
301 model is initialized with two species for which their total mass is constant everywhere (constant  
302 surface pressure and constant mixing ratio  $4 \times 10^{-6}$  kg/kg), such that if tracer mass is conserved,  
303 then the column integrated sum of the species should not vary in time. Figure 7 provides a snapshot  
304 of the mass-weighted, vertically integrated tracer mass at day 15. In CAM-SE, the tracer mass is  
305 not conserved by day 15 and the field is populated by overshoots and undershoots. In contrast, by  
306 day 15, CAM-SE-CSLAM still conserves tracer mass to within machine precision, consistent with  
307 the previous results of this test-case initialized with a dry baroclinic wave (Lauritzen et al. 2017).

308 *b. Aqua-planets*

309 Two year long aqua-planet simulations are performed using CAM-SE and CAM-SE-CSLAM,  
310 using the CAM4 physics package (Neale et al. 2010), as discussed in Section 2. Away from the  
311 grid-scale, the mean states in the two models are very similar. Figure 8 shows the zonal-mean cli-  
312 matological precipitation rates in CAM-SE and CAM-SE-CSLAM. Considering how sensitive this

313 aqua-planet configuration is to design choices in CAM-SE (Lauritzen et al. 2018), it is somewhat  
314 unexpected that the zonal means look so similar to one another.

315 A plot similar to Figure 3a is constructed for the CAM-SE-CSLAM simulation, a probability  
316 density distribution of upward  $\omega$  conditionally sampled based on location within the element. Like  
317 Figure 3a, Figure 3b divides up the control volumes by corner, edge and interior cells. Through the  
318 use of the quasi-equal area physics grid, the dynamical core state appears more or less independent  
319 of location within the element, a marked improvement over CAM-SE. Since the state is approxi-  
320 mately independent of in-element location, it follows that the physics forcing, which is evaluated  
321 from the dynamical core state, may be expected to also show an improvement in grid-imprinting.

322 The low-level, mean and variance of the temperature tendencies from the physics in the two sim-  
323 ulations are shown in Figure 9. The mean states in the two models resemble one another, consistent  
324 with the zonal mean precipitaiton rates (Figure 8). The mean physics tendencies contains modest  
325 grid imprinting in CAM-SE (barely visible near the storm-track regions), while in the variance  
326 field, grid imprinting is both ubiquitous and unmistakable. The variance is larger on boundary  
327 nodes, manifesting as a ‘stitching’ pattern resembling the cube-sphere grid. In CAM-SE-CSLAM,  
328 the grid imprinting is all but eliminated based on the mean and variance of the physics tendencies  
329 (Figure 9), consistent with our expectation.

330 As stated in Section 3, the mapping of the state to the physics grid and the reverse interpolation  
331 of physics tendencies to the GLL grid is not total energy conserving. CAM has a global energy  
332 fixer (Williamson et al. 2015) which can be used to estimate the errors associated with the mapping  
333 algorithms. To do so, it is presumed that there are no compensating mapping errors in going to  
334 and from the physics and dynamics grids, and that CAM-SE-CSLAM and CAM-SE have the same  
335 energy dissipation rates. Under these assumptions the spurious globally integrated total energy  
336 errors due to the mapping algorithm is estimated to be approximately  $0.0025 \text{ W/m}^2$  in the aqua-

337 planet simulations. In comparison, the dynamical core total energy dissipation is on the order of  
338  $0.1 \text{ W/m}^2$  (Lauritzen et al. 2018).

339 *c. Held-Suarez with Topography*

340 Grid imprinting associated with the flow around obstacles is more problematic than that en-  
341 countered on the aqua-planets. In order to diagnose grid imprinting due to topographic flow, an  
342 idealized held-Suarez configuration (Held and Suarez 1994) is outfitted with real world topogra-  
343 phy after Fox-Rabinovitz et al. (2000); Baer et al. (2006), and run for two years. Figure 10 shows  
344 the mean  $\omega$  at two different vertical levels in the middle troposphere. **The data are presented as a**  
345 **raster plot on their respective unstructured grids, in order to delineate whether a particular value is**  
346 **associated with an interior, edge or element boundary node.**

347 At higher latitudes (e.g., the southern Andes), the flow is smooth, conforming reasonably to the  
348 underlying topography. At lower latitudes (within 20 to 30 degrees from the equator), over the  
349 Andes or the Himalayas, there is a clear preference for extrema to occur at the element bound-  
350 aries (Figure 10). The vertical structure of  $\omega$  in regions of strong grid-imprinting indicates full-  
351 troposphere upward/downward motion (not shown). Grid imprinting is therefore more common  
352 in regions of weak stratification, such as occurs in the deep tropics, with forced up-slope flow  
353 facilitating the release of gravitational instability. Resolved updrafts/downdrafts often align with  
354 the element boundaries due to its systematically tighter pressure gradients.

355 Through the use of the quasi-equal area physics grid, grid imprinting due to topographic flow is  
356 reduced (Figures 10). Figure 10 also shows the state in CAM-SE-CSLAM, but on the GLL grid.  
357 Arguably, grid imprinting due to topography in CAM-SE-CSLAM is not much of an improvement  
358 over CAM-SE, viewed from the GLL grid. The native topography lives on the physics grid, and the  
359 topography is mapped to the nodal points at run-time in CAM-SE-CSLAM. Mapping topography

360 to the quadrature nodes ensures that no new extrema will be introduced to the boundary nodes,  
361 where the solution is least smooth. This effect can not be very large, since the grid noise is similar  
362 in CAM-SE and CAM-SE-CSLAM on the GLL grid. From the perspective of the physics grid,  
363 the CAM-SE-CSLAM solution clearly mitigates the influence of grid-induced extrema on the state  
364 (Figure 10). The reduction in grid imprinting in CAM-SE-CSLAM is therefore almost entirely a  
365 result of the smoothing effect of integrating the basis functions over the control volumes of the  
366 physics grid.

367 *d. AMIP type simulations*

368 A pair of 20 year-long AMIP type simulations are performed, using CAM, version 6 physics  
369 package (CAM6) and using perpetual year 2000 SST boundary conditions (*F2000climo* compset  
370 in CESM2.0; <https://doi.org/10.5065/D67H1H0V>). Figure 11 shows the climatological pre-  
371 cipitation fields in CAM-SE (left) and CAM-SE-CSLAM (middle), and over the same mountain-  
372 ous regions as in Figure 10. The plots have some similar features to the  $\omega$  field in the Held-Suarez  
373 runs; the greater variance at lower latitudes, and on the windward side of the mountains are broadly  
374 similar. CAM-SE-CSLAM has a lower spatial variance, e.g., the lack of extrema over the Andes  
375 at about 15° S compared to CAM-SE, and the grid-scale precipitation peak over the Himalayas  
376 at about 30° N. The difference plot (Figure 11; right panel) is more broadly populated by blue,  
377 purple and white contours, indicating that CAM-SE has, in general, lower magnitude precipitation  
378 rates over high topography. The difference plots also highlight a couple of zonally aligned strips  
379 of anomalous precipitation, in particular, near the foot of the Himalayas in CAM-SE. These bands  
380 are in the same location as the bands of precipitation identified in CAM-SE in Lauritzen et al.  
381 (2015a) (their Figure 7), but using CAM, version 5 physics, of which they argue are spurious in  
382 nature.

383 To assist in identifying whether a particular precipitation pattern is spurious, an AMIP type sim-  
384 ulation is carried out using the finite-volume dynamical core that uses a regular latitude-longitude  
385  $1^\circ$  grid (CAM-FV; Neale et al. 2012). CAM-FV is the default low resolution model in CESM2.0,  
386 and with its smoothly varying grid, does not suffer from the Quadrature Node Problem. Figure 12  
387 shows the global precipitation fields in CAM-SE, CAM-SE-CSLAM and CAM-FV, compared to  
388 an observational dataset, the GPCP (1979-2003) gridded dataset (Huffman et al. 2001). The mag-  
389 nitude of the precipitation rates in all three models are higher than the GPCP dataset (note the  
390 lack of red contours in the GPCP dataset), which should be interpreted cautiously due to widely-  
391 accepted issues in constructing a reliable, gridded, global precipitation dataset. At lower latitudes,  
392 CAM-FV has lower spatial variance, and overall lower magnitudes, compared with CAM-SE. The  
393 GPCP dataset and CAM-FV together indicate that perhaps the precipitation rates in CAM-SE are  
394 larger than in reality. Following suit, the reduction in magnitude and spatial variance in precipita-  
395 tion in CAM-SE-CSLAM may be interpreted as an improvement over CAM-SE.

## 396 5. Conclusions

397 Element-based high-order Galerkin Methods possess many of the attractive qualities recom-  
398 mended for next generation global atmospheric models. Among these, high-order accuracy is  
399 achieved with minimal communication between elements, allowing for near perfect scaling on  
400 massively parallel systems. Element communication amounts to a numerical flux applied to the  
401 element boundaries, reconciling overlapping solutions of adjacent elements but degrading the  
402 smoothness of the boundary nodes in the process (to  $C^0$ ). For non-smooth problems, gradients are  
403 systematically tighter at the element boundaries, and local extrema often characterize the boundary  
404 nodes. This behavior is illustrated using NCAR's Community Atmosphere Model with Spectral

405 Elements dynamics (CAM-SE) in an aqua-planet configuration, in a Held-Suarez configuration  
406 with real-world topography **and in an AMIP type configuration.**

407 The authors argue that the conventional physics-dynamics coupling paradigm, in which the  
408 physical parameterizations are evaluated on the dynamical core grid, exacerbates grid imprinting.

409 A separate physics grid is proposed and implemented in CAM-SE, and referred to as CAM-SE-  
410 CSLAM, through dividing the elements into quasi-equal areas with equivalent degrees of freedom.

411 The state is mapped to the physics grid with high-order accuracy through integrating CAM-SE's  
412 Lagrange basis functions over the control volumes. Control volumes near element boundaries now

413 represent a state in the vicinity of the extrema produced through the boundary exchange, as op-  
414 posed to the the nodal value itself. These control volumes are also compatible with a 'large-scale

415 state' as required by the physical parameterizations. The physical parameterizations are evalu-  
416 ated on the finite volume grid, and the forcing terms are mapped back to the dynamical core grid

417 using a cubic tensor-product Lagrange interpolation. In aqua-planet simulations, evaluating the  
418 parameterizations on the physics grid removes any obvious dependence of proximity to the ele-

419 ment boundary, resulting in a more realistic state with negligible grid imprinting. The mapping  
420 algorithm does not conserve total energy, but it is estimated that these errors are one to two orders  
421 of magnitude less than the total energy dissipation from the dynamical core.

422 In CAM-SE-CSLAM, the physics grid replaces the default CAM-SE quadrature point-based  
423 coupler grid (Figure 4) to compute fluxes between model components in the Community Earth

424 System Model (CESM). The appeal here is two-fold. Through integrating the Lagrange basis  
425 functions over control volumes, one can be certain that the fluxes computed from this grid are  
426 a volume averaged flux. The same can not be said for CAM-SE, where the nodal values are

427 effectively assigned to each control volume. The second advantage of the new coupler grid is  
428 that extrema occurring on boundary nodes may no longer influence other model components, in

429 simulations without rough topography. While grid imprinting is effectively eliminated in the aqua-  
430 planets, experiments with real-world topography (Held-Suarez and AMIP type configurations)  
431 reduces, but does not entirely eliminate, imprinting from the mean state. The quasi-equal area  
432 physics grid is nonetheless effective at mitigating numerical nuances associated with high-order  
433 element-based Galerkin methods, for non-smooth problems.

434 *Acknowledgments.* NCAR is sponsored by the National Science Foundation (NSF). We thank  
435 three anonymous reviewers for their helpful comments that significantly improved the clarity of  
436 the manuscript. Herrington thanks NCAR’s Computational and Information Systems Laboratory  
437 (CISL) and NCAR’s Climate and Global Dynamics division (CGD) for computational resources  
438 and technical support. Herrington, Reed, and Lauritzen are grateful to the NCAR Advanced Study  
439 Program graduate visitor program for funding Herrington’s 12-month visit. Goldhaber was par-  
440 tially supported by the Accelerated Climate Modeling for Energy (ACME) project, and work pack-  
441 age 12 – 015334 “Multiscale Methods for Accurate, Efficient, and the Accelerated Scale-Aware  
442 Models, both funded through the U.S. Department of Energy Office of Biological and Environ-  
443 mental Resarch. Goldhaber is also partially supported through NSF award AGS-1500187 “De-  
444 velopment and Testing of a Global Quasi 3-D multi Modeling Framework.” Model source code is  
445 officially released with CESM2.1 (<https://doi.org/10.5065/D67H1H0V>).

446 APPENDIX

447 The mapping of the physics tendencies from the physics grid to the GLL grid is done with  
448 tensor-cubic Lagrange interpolation. The elements of the cubed-sphere in SE are created  
449 from an equi-angular gnomonic projection. Consider one element  $(\alpha, \beta) \in [\alpha_1^{(elem)}, \alpha_2^{(elem)}] \times$   
450  $[\beta_1^{(elem)}, \beta_2^{(elem)}]$ , where  $(\alpha, \beta)$  are central angle coordinates and  $\alpha_1^{(elem)}$  and  $\alpha_2^{(elem)}$  are the min-  
451 imum and maximum central angles in the  $\alpha$ -coordinate direction, respectively, and similarly for

<sup>452</sup>  $\beta$ . Let  $\Delta\alpha^{(elem)} = \alpha_2^{(elem)} - \alpha_1^{(elem)}$  and  $\Delta\beta^{(elem)} = \beta_2^{(elem)} - \beta_1^{(elem)}$ . The physics grid cell central  
<sup>453</sup> angle centers are located at

$$(\alpha_i^{(pg)}, \beta_j^{(pg)}) = \left[ \alpha_1^{(elem)} + (i - \frac{1}{2}) \Delta\alpha^{(pg)}, \right. \\ \left. \beta_1^{(elem)} + (j - \frac{1}{2}) \Delta\beta^{(pg)} \right], \quad (\text{A1})$$

<sup>454</sup> where  $\Delta\alpha^{(pg)} = \Delta\beta^{(pg)} = \frac{\Delta\alpha^{(elem)}}{pg} = \frac{\Delta\beta^{(elem)}}{pg}$ . The interpolation is performed in central-angle co-  
<sup>455</sup> ordinates using tensor product cubic interpolation. For elements located on a cubed-sphere edge  
<sup>456</sup> or corner the coordinate system for neighboring elements may be on a different panel. To take  
<sup>457</sup> into account this coordinate change the central angle locations of physics grid cell centers located  
<sup>458</sup> on other panels are transformed to the coordinate system of the panel the element in question is  
<sup>459</sup> located on (the transformations are given in, e.g., Nair et al. 2005). An illustration is given in  
<sup>460</sup> Figure 13 for an element located in the lower left corner of a panel. The element in question is  
<sup>461</sup>  $(\xi, \chi) \in (-1, 1)^2$  where, for simplicity, we have transformed the element coordinates into normal-  
<sup>462</sup> ized coordinates  $(\xi, \chi) = \left( \frac{2(\alpha^{(pg)} - \alpha_1^{(elem)})}{\Delta\alpha^{(elem)}} - 1, \frac{2(\beta^{(pg)} - \beta_1^{(elem)})}{\Delta\beta^{(elem)}} - 1 \right)$ ; also used internally in the  
<sup>463</sup> SE dynamical core (see, e.g., section 3.3 in Lauritzen et al. 2018). The GLL points are located at  
<sup>464</sup>  $-1, -\sqrt{5}/5, \sqrt{5}/5$ , and  $1$  in each coordinate direction. Near the edges/corners of an element cubic  
<sup>465</sup> extrapolation is used if the centered stencil expands beyond the panel.

## <sup>466</sup> References

- <sup>467</sup> Arakawa, A., and W. H. Schubert, 1974: Interaction of a cumulus cloud ensemble with the large-  
<sup>468</sup> scale environment, Part I. *J. Atmos. Sci.*, **31**, 674–701.
- <sup>469</sup> Bacmeister, J. T., K. A. Reed, C. Hannay, P. Lawrence, S. Bates, J. E. Truesdale, N. Rosen-  
<sup>470</sup> bloom, and M. Levy, 2018: Projected changes in tropical cyclone activity under future warm-

- 471 ing scenarios using a high-resolution climate model. *Climatic Change*, **146**, 547–560, doi:  
472 10.1007/s10584-016-1750-x, URL <http://dx.doi.org/10.1007/s10584-016-1750-x>.
- 473 Baer, F., H. Wang, J. J. Tribbia, and A. Fournier, 2006: Climate modeling with spectral elements.  
474 *Mon. Wea. Rev.*, **134**, 3610–3624, doi:10.1175/MWR3360.1, URL <http://dx.doi.org/10.1175/MWR3360.1>.
- 475 Brdar, S., M. Baldauf, A. Dedner, and R. Klöfkorn, 2013: Comparison of dynamical cores for  
476 nwp models: comparison of cosmo and dune. *Theoretical and Computational Fluid Dynamics*,  
477 **27** (3-4), 453–472, doi:10.1007/s00162-012-0264-z.
- 478 Canuto, C., M. Y. Hussaini, A. Quarteroni, and T. Zang, 2007: *Spectral Methods: Evolution to  
Complex Geometries and Applications to Fluid Dynamics*. 1st ed., Springer.
- 479 Dennis, J. M., and Coauthors, 2012: CAM-SE: A scalable spectral element dynamical core for  
480 the Community Atmosphere Model. *Int. J. High. Perform. C.*, **26** (1), 74–89, doi:10.1177/  
481 1094342011428142, URL <http://hpc.sagepub.com/content/26/1/74.abstract>, <http://hpc.sagepub.com/content/26/1/74.full.pdf+html>.
- 482 Durran, D., 2010: *Numerical Methods for Fluid Dynamics: With Applications to Geophysics*,  
483 Texts in Applied Mathematics, Vol. 32. 2nd ed., Springer, 516 p.
- 484 Fournier, A., M. A. Taylor, and J. J. Tribbia, 2004: The spectral element atmosphere model  
485 (SEAM): High-resolution parallel computation and localized resolution of regional dynamics.  
486 *Mon. Wea. Rev.*, **132** (3), 726–748.
- 487 Fox-Rabinovitz, M. S., G. L. Stenchikov, M. J. Suarez, L. L. Takacs, and R. C. Govindaraju, 2000:  
488 A uniform- and variable-resolution stretched-grid gcm dynamical core with realistic orography.  
489 *Mon. Wea. Rev.*, **128**, 1883–1898.

- 493 Giraldo, F., and M. Restelli, 2008: A study of spectral element and discontinuous galerkin methods  
494 for the Navier-Stokes equations in nonhydrostatic mesoscale atmospheric modeling: Equation  
495 sets and test cases. *J. Comput. Phys.*, **227** (8), 3849 – 3877, doi:<http://dx.doi.org/10.1016/j.jcp>.  
496 2007.12.009.
- 497 Guba, O., M. Taylor, and A. St-Cyr, 2014a: Optimization-based limiters for the spectral element  
498 method. *J. Comput. Phys.*, **267** (0), 176 – 195, doi:<http://dx.doi.org/10.1016/j.jcp.2014.02.029>.
- 499 Guba, O., M. A. Taylor, P. A. Ullrich, J. R. Overfelt, and M. N. Levy, 2014b: The spectral element  
500 method (sem) on variable-resolution grids: evaluating grid sensitivity and resolution-aware nu-  
501 matical viscosity. *Geosci. Model Dev.*, **7** (6), 2803–2816, doi:[10.5194/gmd-7-2803-2014](https://doi.org/10.5194/gmd-7-2803-2014).
- 502 Held, I. M., and M. J. Suarez, 1994: A proposal for the intercomparison of the dynamical cores of  
503 atmospheric general circulation models. *Bull. Am. Meteorol. Soc.*, **73**, 1825–1830.
- 504 Huffman, G. J., R. F. Adler, M. M. Morrissey, D. T. Bolvin, S. Curtis, R. Joyce, B. McGavock,  
505 and J. Susskind, 2001: Global precipitation at one-degree daily resolution from multisatellite  
506 observations. *J. Hydrometeorology*, **2** (1), 36–50.
- 507 Kessler, E., 1969: On the distribution and continuity of water substance in atmospheric circula-  
508 tions. *Meteorol. Monogr.*, **10** (32), 88.
- 509 Kim, Y.-J., F. X. Giraldo, M. Flatau, C.-S. Liou, and M. S. Peng, 2008: A sensitivity study of the  
510 kelvin wave and the Madden-Julian oscillation in aquaplanet simulations by the Naval Research  
511 Laboratory Spectral Element Atmospheric Model. *J. Geo. Res.: Atmospheres*, **113** (D20), doi:  
512 [10.1029/2008JD009887](https://doi.org/10.1029/2008JD009887), d20102.

- 513 Lauritzen, P. H., J. T. Bacmeister, P. F. Callaghan, and M. A. Taylor, 2015a: Ncar global model  
514 topography generation software for unstructured grids. *Geoscientific Model Development Discussions*, **8** (6), 4623–4651, doi:10.5194/gmdd-8-4623-2015.
- 515
- 516 Lauritzen, P. H., A. J. Conley, J.-F. Lamarque, F. Vitt, and M. A. Taylor, 2015b: The terminator  
517 “toy” chemistry test: a simple tool to assess errors in transport schemes. *Geoscientific Model  
518 Development*, **8** (5), 1299–1313, doi:10.5194/gmd-8-1299-2015.
- 519 Lauritzen, P. H., M. A. Taylor, J. Overfelt, P. A. Ullrich, R. D. Nair, S. Goldhaber, and  
520 R. Kelly, 2017: CAM-SE-CSLAM: Consistent coupling of a conservative semi-lagrangian  
521 finite-volume method with spectral element dynamics. *Mon. Wea. Rev.*, **145** (3), 833–855, doi:  
522 10.1175/MWR-D-16-0258.1.
- 523 Lauritzen, P. H., and Coauthors, 2018: Ncar cesm2.0 release of cam-se: A reformulation of the  
524 spectral-element dynamical core in dry-mass vertical coordinates with comprehensive treatment  
525 of condensates and energy. *J. Adv. Model. Earth Syst.*, doi:10.1029/2017MS001257.
- 526 Lin, S.-J., 2004: A ‘vertically Lagrangian’ finite-volume dynamical core for global models. *Mon.  
527 Wea. Rev.*, **132**, 2293–2307.
- 528 Maday, Y., and A. T. Patera, 1987: Spectral element methods for the incompressible Navier Stokes  
529 equations. *State of the Art Surveys on Computational Mechanics*, A. K. Noor, and J. T. Oden,  
530 Eds., ASME, New York, 71–143.
- 531 Medeiros, B., D. L. Williamson, and J. G. Olson, 2016: Reference aquaplanet climate in the  
532 community atmosphere model, version 5. *J. Adv. Model. Earth Syst.*, **8** (1), 406–424, doi:10.  
533 1002/2015MS000593.

- 534 Nair, R., H.-W. Choi, and H. Tufo, 2009: Computational aspects of a scalable high-order dis-  
535 continuous galerkin atmospheric dynamical core. *Computers & Fluids*, **38** (2), 309 – 319, doi:  
536 <http://dx.doi.org/10.1016/j.compfluid.2008.04.006>.
- 537 Nair, R. D., M. N. Levy, and P. H. Lauritzen, 2011: Emerging numerical methods for atmo-  
538 spheric modeling, in: P.H. Lauritzen, R.D. Nair, C. Jablonowski, M. Taylor (Eds.), Numerical  
539 techniques for global atmospheric models. *Lecture Notes in Computational Science and Engi-  
540 neering, Springer*, **80**.
- 541 Nair, R. D., S. J. Thomas, and R. D. Loft, 2005: A discontinuous galerkin transport scheme on the  
542 cubed sphere. *Mon. Wea. Rev.*, **133** (4), 814–828, doi:10.1175/MWR2890.1.
- 543 Neale, R. B., and B. J. Hoskins, 2000: A standard test for agcms including their physical  
544 parametrizations: I: the proposal. *Atmos. Sci. Lett.*, **1** (2), 101–107, doi:10.1006/asle.2000.0022.
- 545 Neale, R. B., and Coauthors, 2010: Description of the NCAR Community Atmosphere Model  
546 (CAM 4.0). NCAR Technical Note, National Center of Atmospheric Research.
- 547 Neale, R. B., and Coauthors, 2012: Description of the NCAR Community Atmosphere Model  
548 (CAM 5.0). NCAR Technical Note NCAR/TN-486+STR, National Center of Atmospheric Re-  
549 search.
- 550 Plant, G. C. C., R. S., 2008: A stochastic parameterization for deep convection based on equilib-  
551 rium statistics. *J. Atmos. Sci.*, **65**, 87–105, doi:10.1175/2007JAS2263.1, URL <http://dx.doi.org/10.1175/2007JAS2263.1>.
- 553 Polvani, L., A. Clement, B. Medeiros, J. Benedict, and I. Simpson, 2017: Opening the door to  
554 simpler climate models in the community earth system model project. *EOS*, submitted.

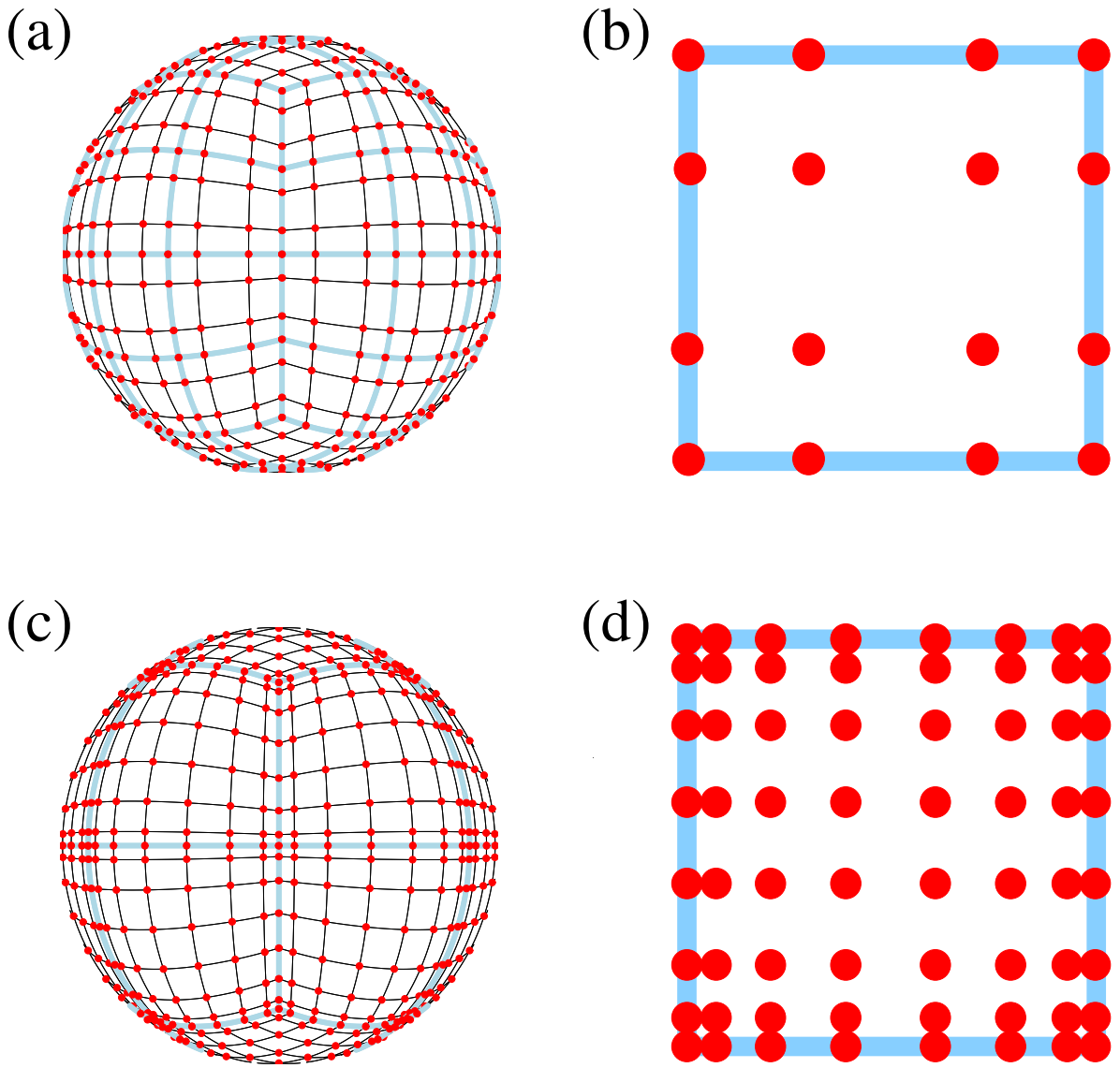
- 555 Putman, W. M., and S.-J. Lin, 2007: Finite-volume transport on various cubed-sphere grids. *J.*  
556 *Comput. Phys.*, **227** (1), 55–78.
- 557 Reed, K. A., J. T. Bacmeister, N. A. Rosenbloom, M. F. Wehner, S. C. Bates, P. H. Lauritzen,  
558 J. E. Truesdale, and C. Hannay, 2015: Impact of the dynamical core on the direct simulation  
559 of tropical cyclones in a high-resolution global model. *Geophys. Res. Lett.*, **42** (9), 3603–3608,  
560 doi:10.1002/2015GL063974.
- 561 Rhoades, A. M., X. Huang, P. A. Ullrich, and C. M. Zarzycki, 2016: Characterizing sierra  
562 nevada snowpack using variable-resolution cesm. *Journal of Applied Meteorology and Cli-*  
563 *matology*, **55** (1), 173–196, doi:10.1175/JAMC-D-15-0156.1, URL <https://doi.org/10.1175/JAMC-D-15-0156.1>.
- 564
- 565 Simmons, A. J., and D. M. Burridge, 1981: An energy and angular-momentum conserving vertical  
566 finite-difference scheme and hybrid vertical coordinates. *Mon. Wea. Rev.*, **109** (4), 758–766.
- 567 Small, R. J., and Coauthors, 2014: A new synoptic scale resolving global climate simulation using  
568 the community earth system model. *Journal of Advances in Modeling Earth Systems*, **6** (4),  
569 1065–1094, doi:10.1002/2014MS000363.
- 570 Suarez, M. J., A. Arakawa, and D. A. Randall, 1983: The parameterization of the planetary  
571 boundary layer in the ucla general circulation model: Formulation and results. *Mon. Wea. Rev.*,  
572 **111** (11), 2224–2243.
- 573 Taylor, M., J. Edwards, and A. St-Cyr, 2008: Petascale atmospheric models for the community  
574 climate system model: new developments and evaluation of scalable dynamical cores. *J. Phys.:  
575 Conf. Ser.*, **125**, doi:10.1088/1742-6596/125/1/012023.

- 576 Taylor, M. A., and A. Fournier, 2010: A compatible and conservative spectral element method on  
577 unstructured grids. *J. Comput. Phys.*, **229** (17), 5879 – 5895, doi:10.1016/j.jcp.2010.04.008.
- 578 Thatcher, D. R., and C. Jablonowski, 2016: A moist aquaplanet variant of the Held–Suarez test  
579 for atmospheric model dynamical cores. *Geoscientific Model Development*, **9** (4), 1263–1292,  
580 doi:10.5194/gmd-9-1263-2016, URL <https://www.geosci-model-dev.net/9/1263/2016/>.
- 581 Ullrich, P. A., 2014: A global finite-element shallow-water model supporting continuous and dis-  
582 continuous elements. *Geosci. Model Dev.*, **7** (6), 3017–3035, doi:10.5194/gmd-7-3017-2014.
- 583 Ullrich, P. A., D. Devendran, and H. Johansen, 2016: Arbitrary-order conservative and consistent  
584 remapping and a theory of linear maps: Part ii. *Mon. Wea. Rev.*, **144** (4), 1529–1549, doi:  
585 10.1175/MWR-D-15-0301.1.
- 586 Ullrich, P. A., T. Melvin, C. Jablonowski, and A. Staniforth, 2014: A proposed baroclinic wave test  
587 case for deep and shallow-atmosphere dynamical cores. *Quart. J. Royal Meteor. Soc.*, **140** (682),  
588 1590–1602.
- 589 Ullrich, P. A., and M. A. Taylor, 2015: Arbitrary-order conservative and consistent remap-  
590 ping and a theory of linear maps: Part I. *Mon. Wea. Rev.*, **143**, 2419–2440, doi:10.1175/  
591 MWR-D-14-00343.1.
- 592 Ullrich, P. A., and Coauthors, 2017: Dcmip2016: A review of non-hydrostatic dynamical core  
593 design and intercomparison of participating models. *Geosci. Model Dev.*, **10**, 4477–4509, doi:  
594 10.5194/gmd-10-4477-2017.
- 595 Wan, H., and Coauthors, 2013: The icon-1.2 hydrostatic atmospheric dynamical core on triangular  
596 grids, part i: formulation and performance of the baseline version. *Geosci. Model Dev.*, **6**, 735–  
597 763.

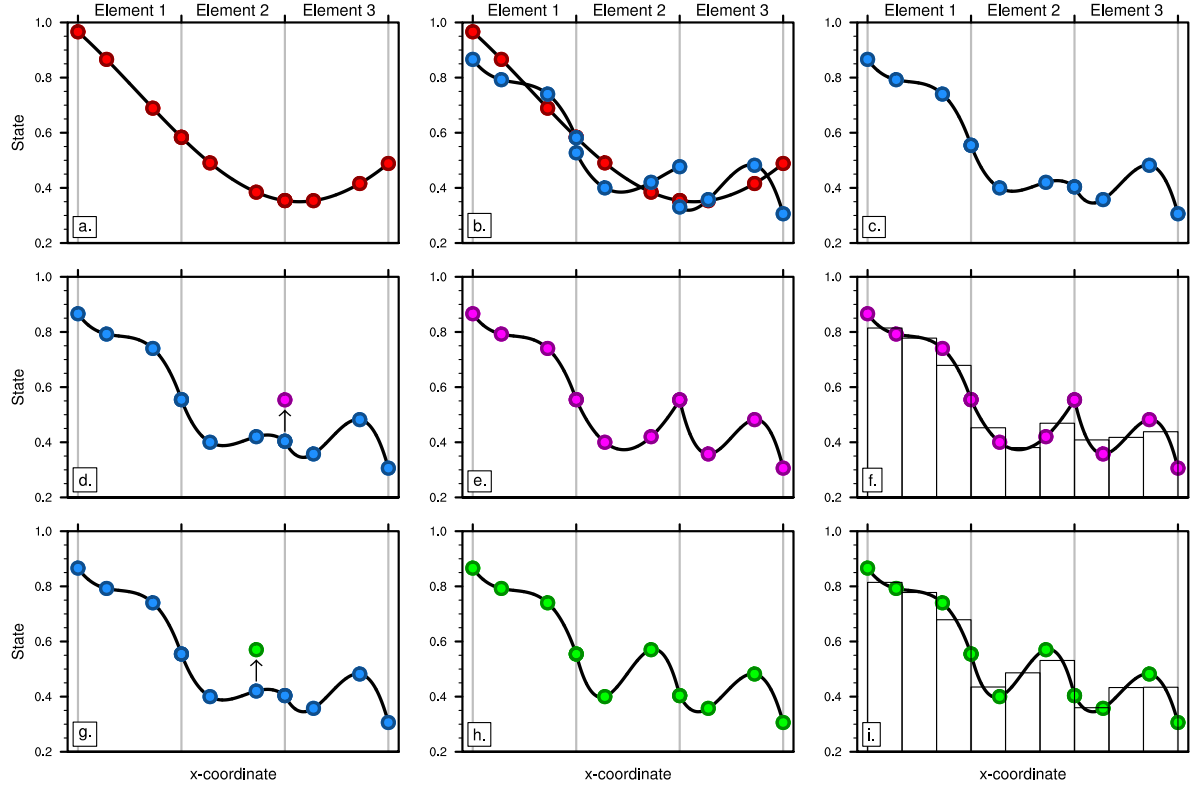
- 598 Williamson, D. L., 2002: Time-split versus process-split coupling of parameterizations and dy-  
599 namical core. *Mon. Wea. Rev.*, **130**, 2024–2041.
- 600 Williamson, D. L., J. G. Olson, C. Hannay, T. Toniazzo, M. Taylor, and V. Yudin, 2015: Energy  
601 considerations in the community atmosphere model (cam). *J. Adv. Model. Earth Syst.*, **7** (3),  
602 1178–1188, doi:10.1002/2015MS000448, URL <http://dx.doi.org/10.1002/2015MS000448>.
- 603 Zarzycki, C. M., C. Jablonowski, and M. A. Taylor, 2014a: Using variable-resolution meshes to  
604 model tropical cyclones in the community atmosphere model. *Mon. Wea. Rev.*, **142** (3), 1221–  
605 1239, doi:10.1175/MWR-D-13-00179.1.
- 606 Zarzycki, C. M., M. N. Levy, C. Jablonowski, J. R. Overfelt, M. A. Taylor, and P. A. Ullrich,  
607 2014b: Aquaplanet experiments using cam’s variable-resolution dynamical core. *J. Climate*,  
608 **27** (14), 5481–5503, doi:10.1175/JCLI-D-14-00004.1.
- 609 Zhang, K., and Coauthors, 2017: Impact of numerical choices on water conservation in the e3sm  
610 atmosphere model version 1 (eam v1). *Geoscientific Model Development Discussions*, **2017**,  
611 1–26, doi:10.5194/gmd-2017-293.

612 LIST OF FIGURES





678 FIG. 1. Example of CAM-SE GLL quadrature grids, marked with red filled circles, (a & c) on the cubed-  
 679 sphere and (b & d) in an element. (a)-(b) and (c)-(d) use  $4 \times 4$  ( $np = 4$ ) and  $8 \times 8$  ( $np = 8$ ) GLL quadrature  
 680 points in each element, respectively. (a) and (c) have the same average grid-spacing at the Equator ( $7.5^\circ$ ) which is  
 681 obtained by using (a)  $4 \times 4$  ( $ne = 4$ ) and (b)  $2 \times 2$  ( $ne = 2$ ) elements on each cubed-sphere face/panel, respectively.  
 682 The element boundaries are marked with thick light blue lines. The grid configurations shown on (a) and (c) are  
 683 referred to as  $ne4np4$  and  $ne2np8$ , respectively.



684 FIG. 2. A one-dimensional schematic showing the relationship between the basis functions, the quadrature  
 685 nodes and the proposed physics grid, over the coarse of a time-step. The filled circles are the GLL quadrature  
 686 points in each element, which are connected by a Lagrange polynomials basis (curves). (a) Smooth initial con-  
 687 dition are (b) advanced by the dynamics one Runge-Kutta step (blue), and (c) shows the solution after applying  
 688 the DSS operator. Applying (d) grid-scale forcing to an element boundary node, (e) the basis representation is  
 689 clearly  $C^0$  at the element boundary. In contrast, (d) applying grid-scale forcing to an interior node (e) results  
 690 in a smooth,  $C^\infty$  continuous field. (f),(i) Vertical bars pertain to the values on the physics grid, found through  
 691 integrating the basis functions over the control volumes.

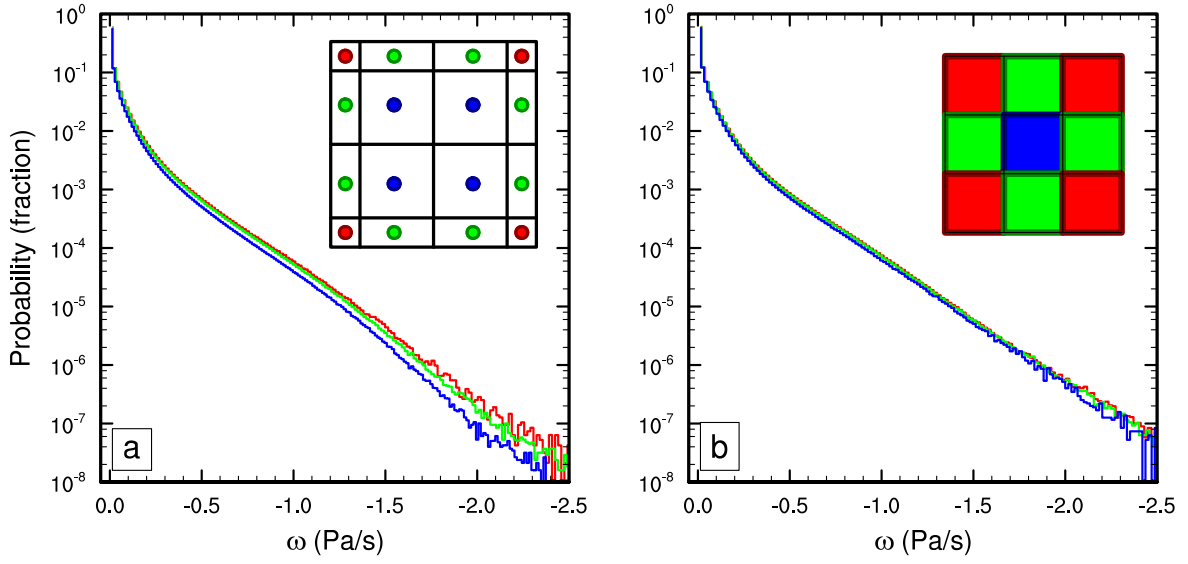
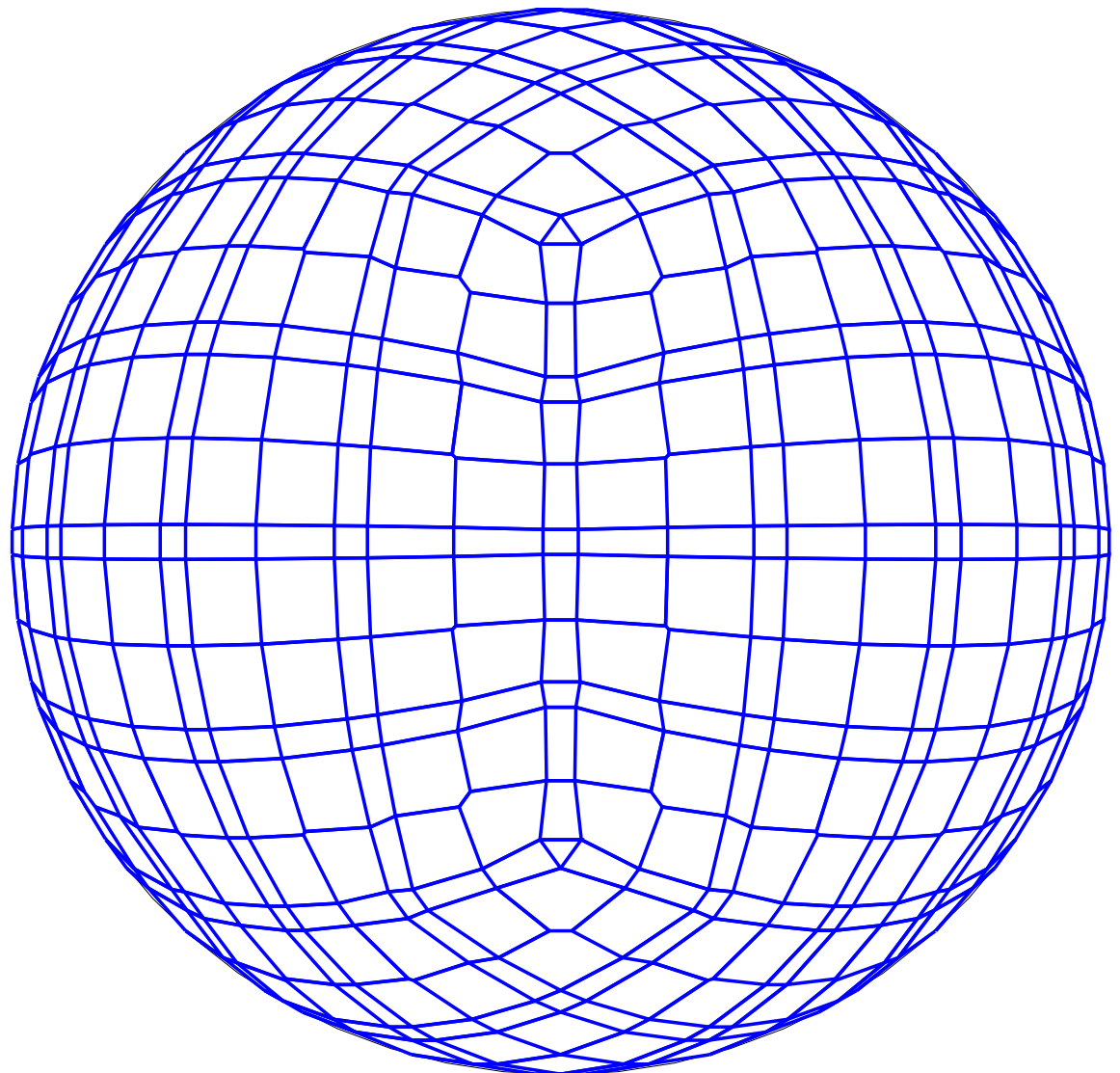
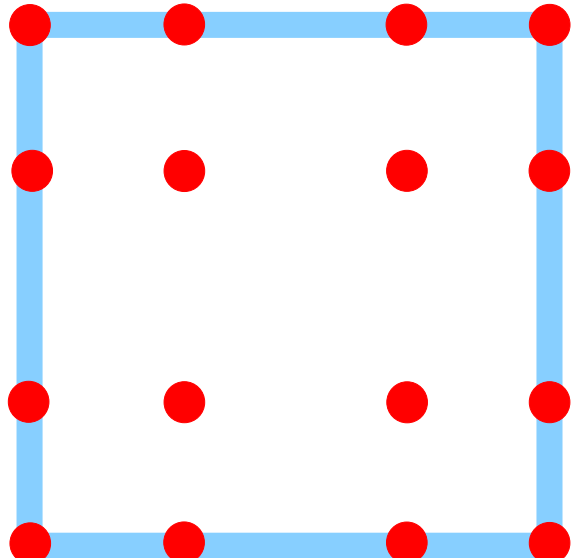


FIG. 3. Probability density distribution of instantaneous upward  $\omega$  in a pair of aqua-planet simulations using CAM4 physics. Figure is constructed from one year of six hourly data, at all vertical levels. (a) *ne30np4* configuration conditionally sampled for interior, edge and corner node control volumes, and similarly (b) for the *ne30pg3* configuration. Note the consistently larger magnitude  $\omega$  for boundary nodes compared with interior nodes in (a), and that the bias is substantially reduced through mapping to a quasi-equal area physics grid.

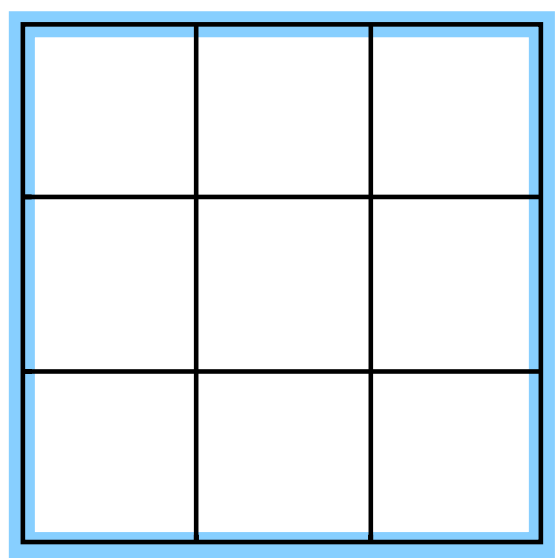


697 FIG. 4. An example of control volumes constructed around GLL quadrature points ( $ne4np4$ ) so that the  
698 spherical area of the control volumes exactly match the quadrature weight multiplied by the metric factor.

$$np = 4$$



$$pg = 3$$



699 FIG. 5. A schematic illustration of an element, indicating the relationship between (left) the dynamical core  
700 grid, and (right) the proposed quasi-equal area physics grid. The physics grid contains  $pg \times pg = 3 \times 3$  grid cells  
701 in each element.

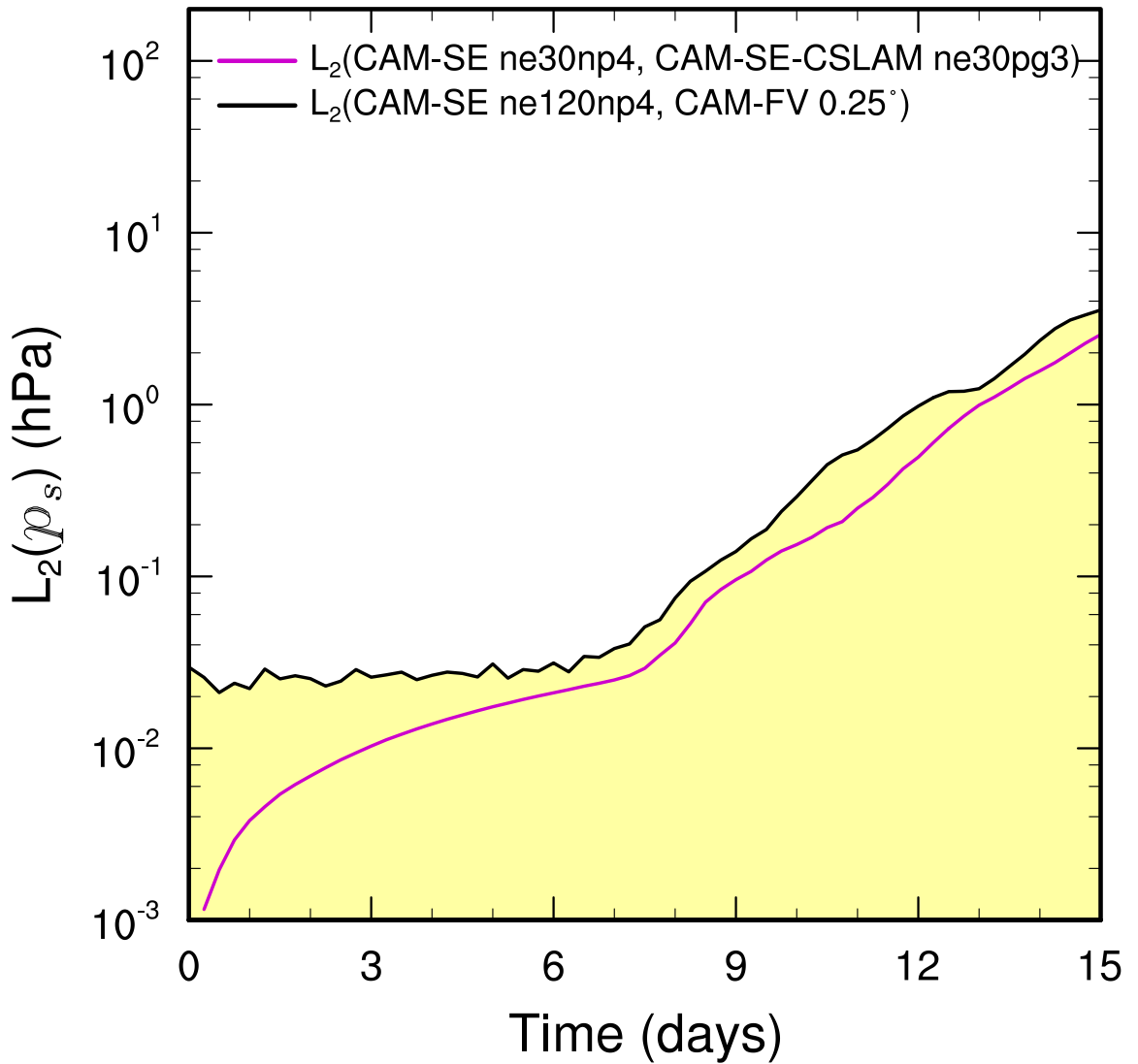
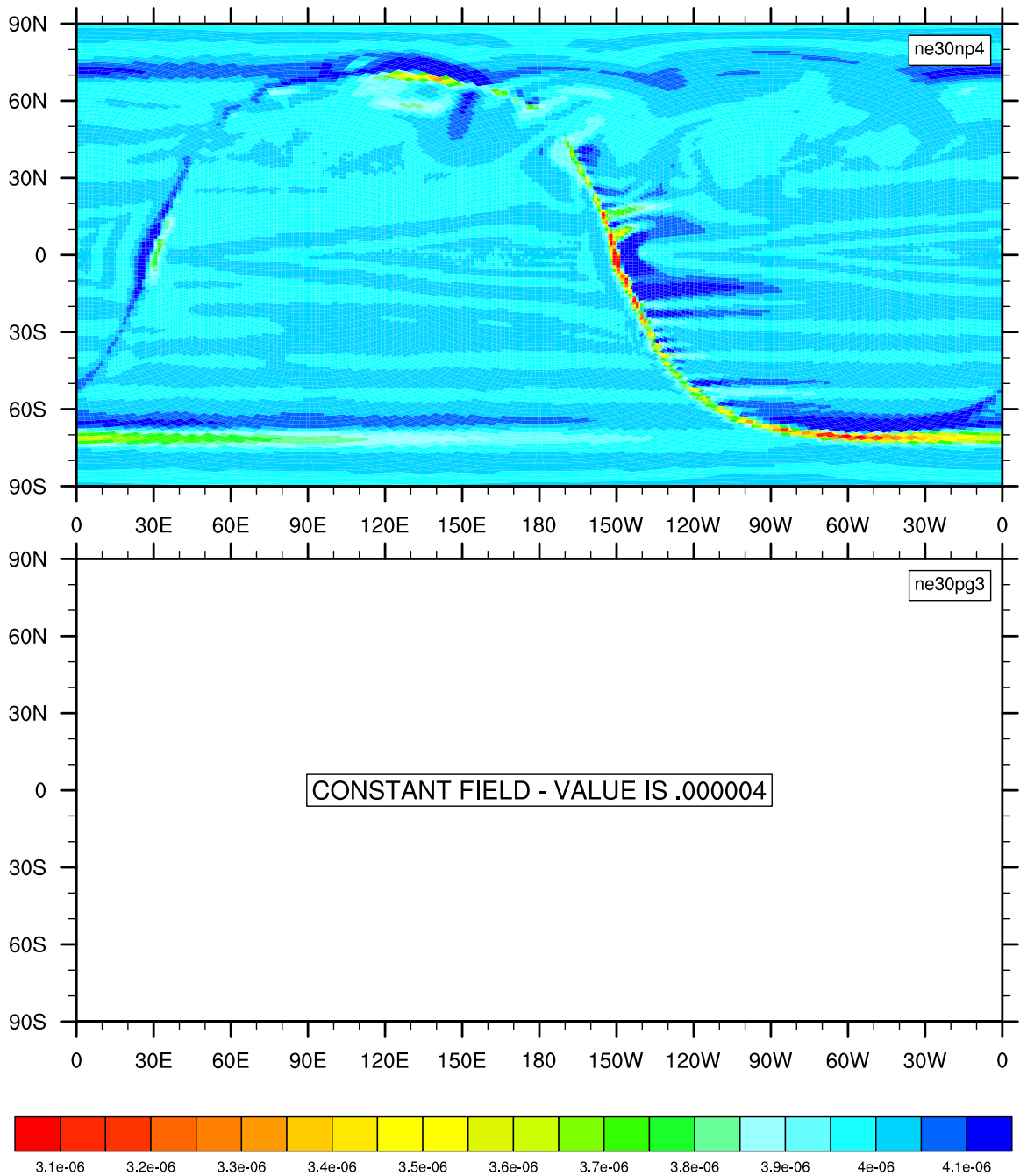
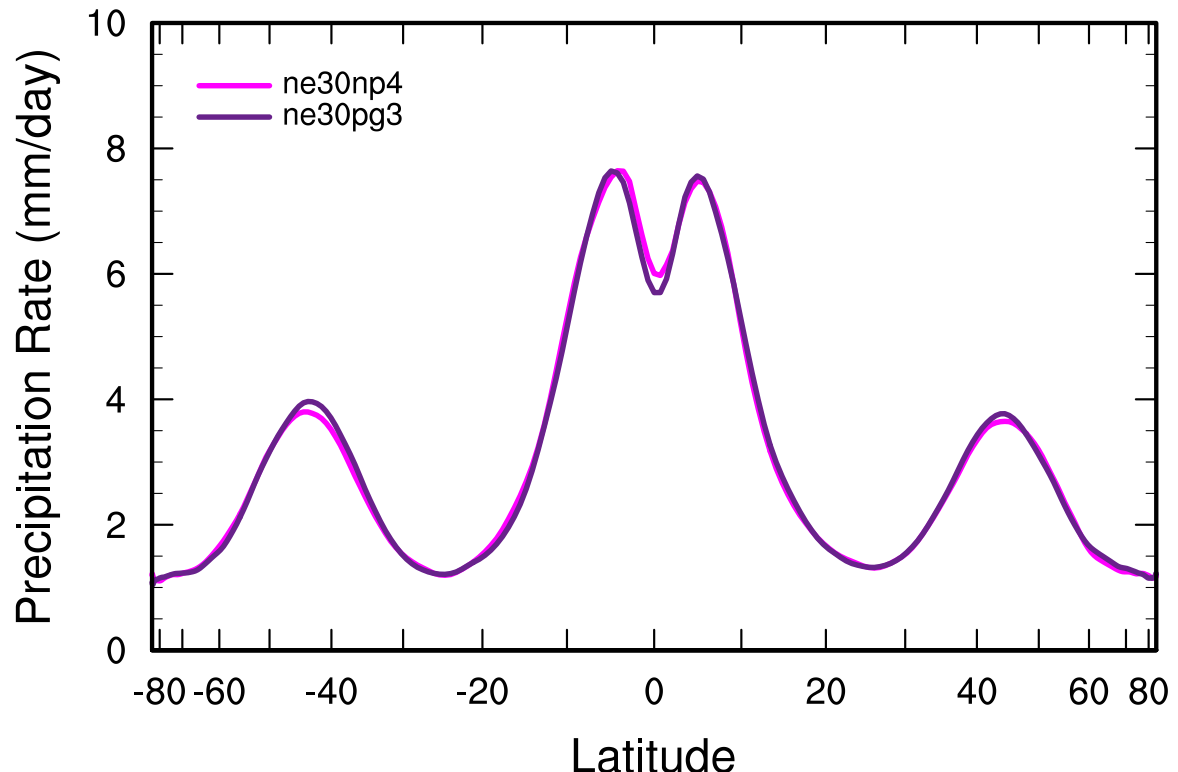


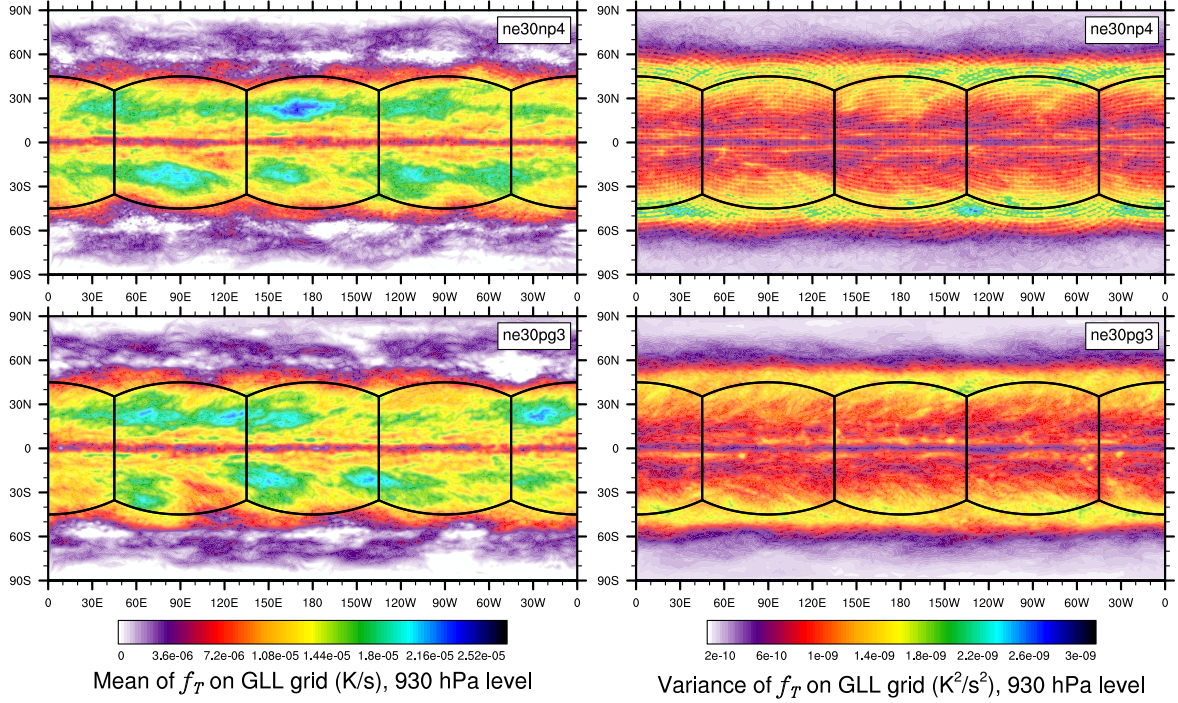
FIG. 6.  $L_2$  difference norms of the surface pressure field,  $p_s$ , in the moist baroclinic wave simulations.  $L_2$  values lying within the yellow region fall below the estimate of the uncertainty in the reference solution (black curve), computed as the difference norm between two approximately  $0.25^\circ$  resolution versions of CAM, the spectral-element and finite-volume (CAM-FV) dynamical cores.



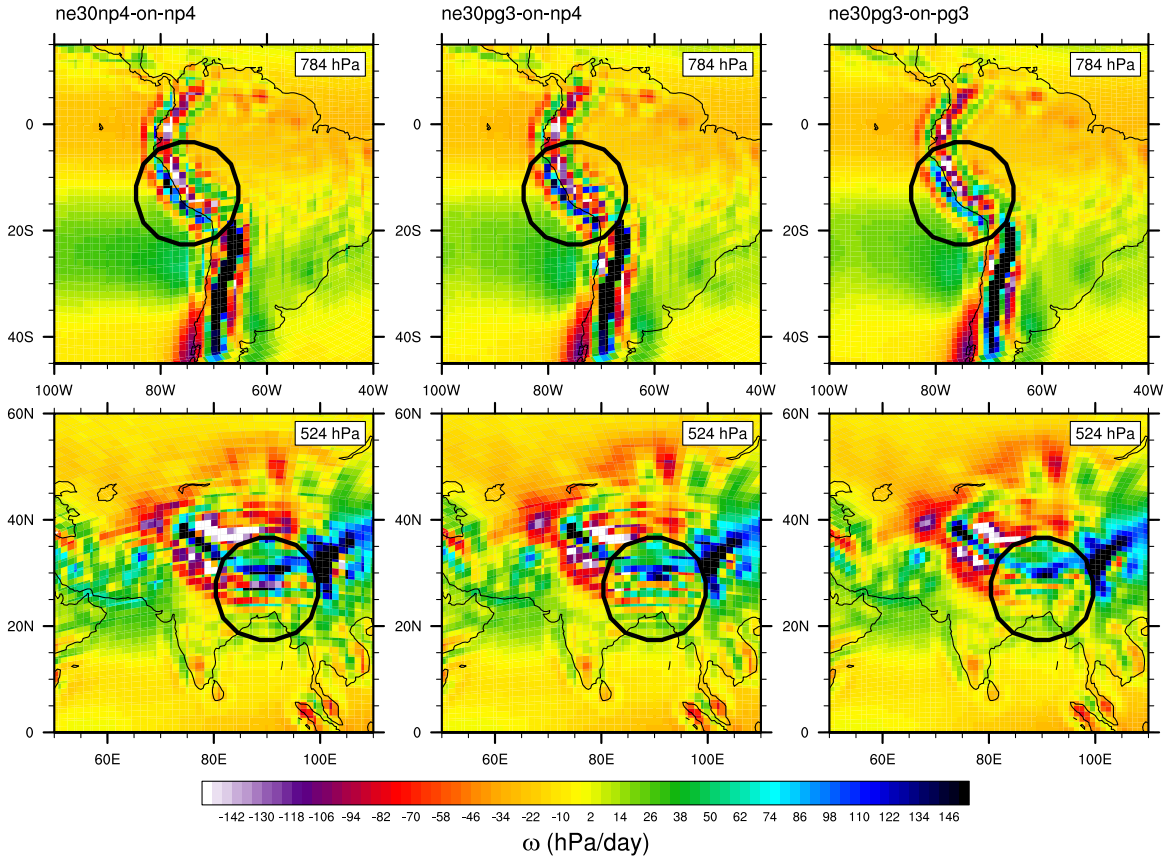
706 FIG. 7. Results of the terminator "toy"-chemistry test. Snapshot of the total column tracer mass at day 15 of  
 707 the moist baroclinic wave test. (Top) CAM-SE, (Bottom) CAM-SE-CSLAM.



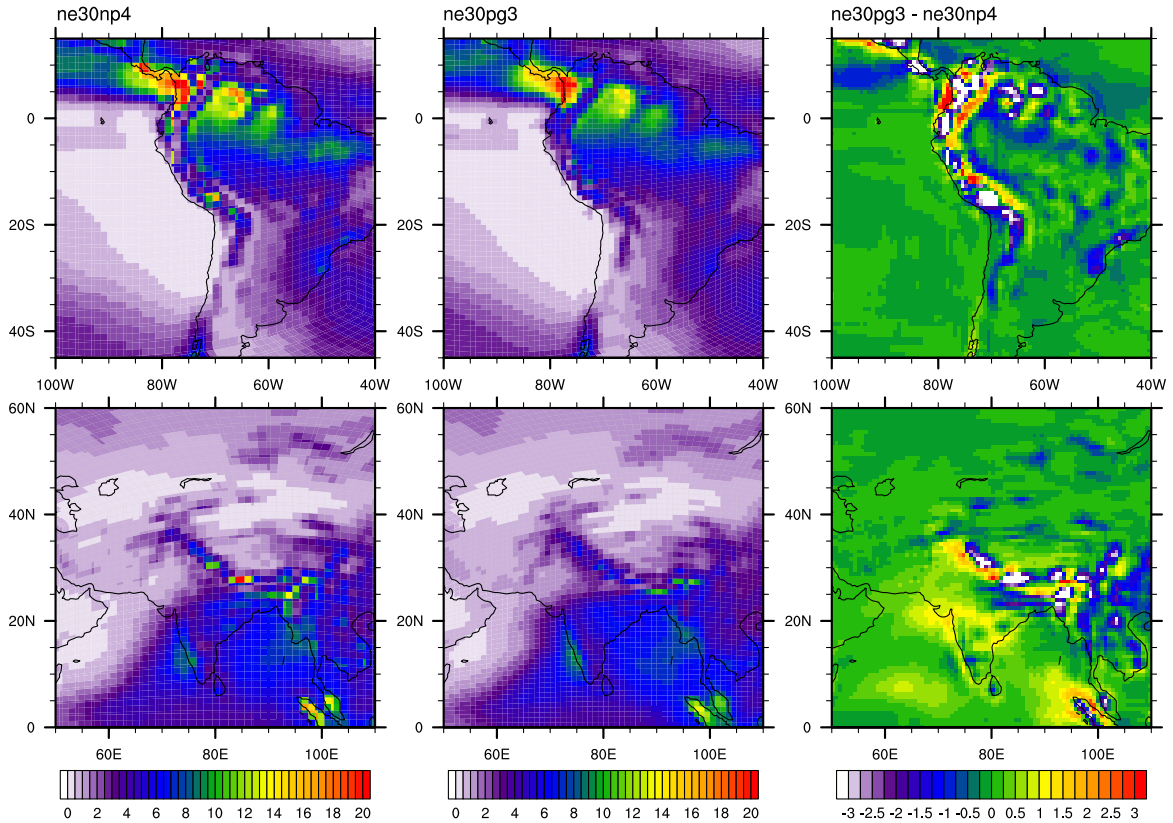
708 FIG. 8. Climatological zonal-mean total precipitation rate in the aqua-planets, computed from a pair of year  
709 long simulations.



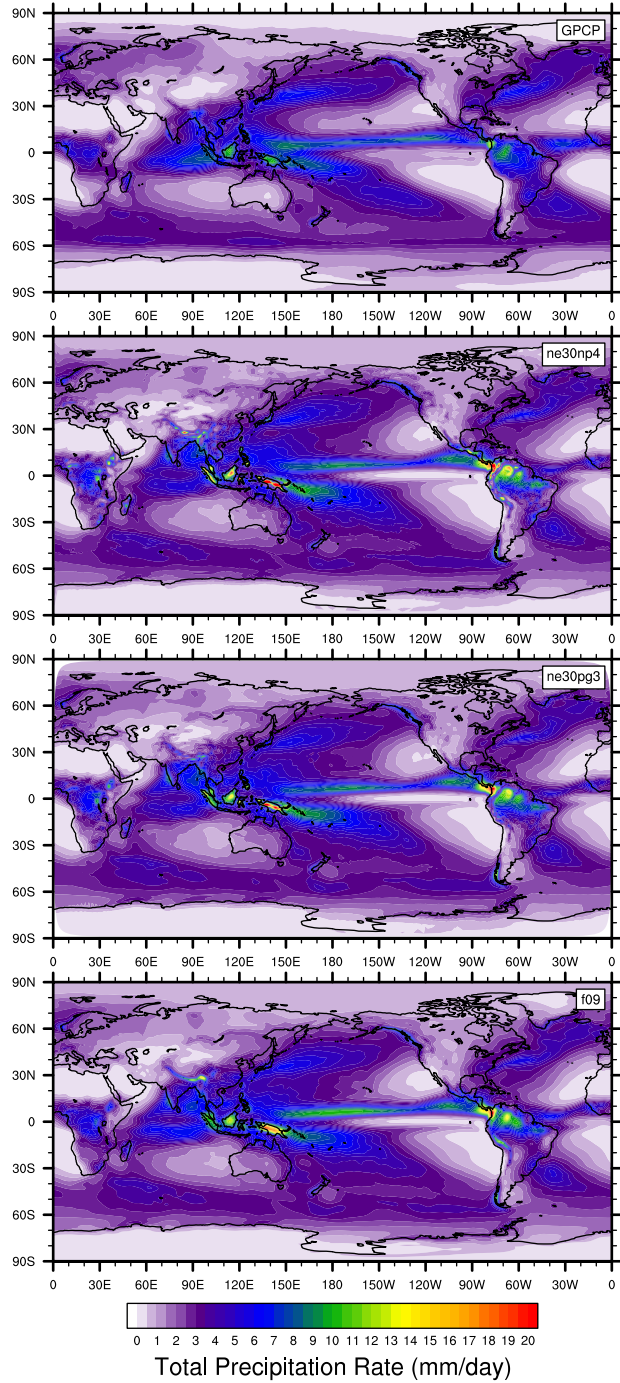
710 FIG. 9. Mean (left) and variance (right) of the low level temperature tendencies from the physical parameteri-  
 711 zations on the GLL grid, with the ne30np4 configuration, (top row) and ne30pg3 configuration (bottom row), in  
 712 a pair of year-long aqua-planet simulations after Medeiros et al. (2016). Grid imprinting is observed along the  
 713 element boundaries in ne30np4, but is absent from the ne30pg3 simulation.



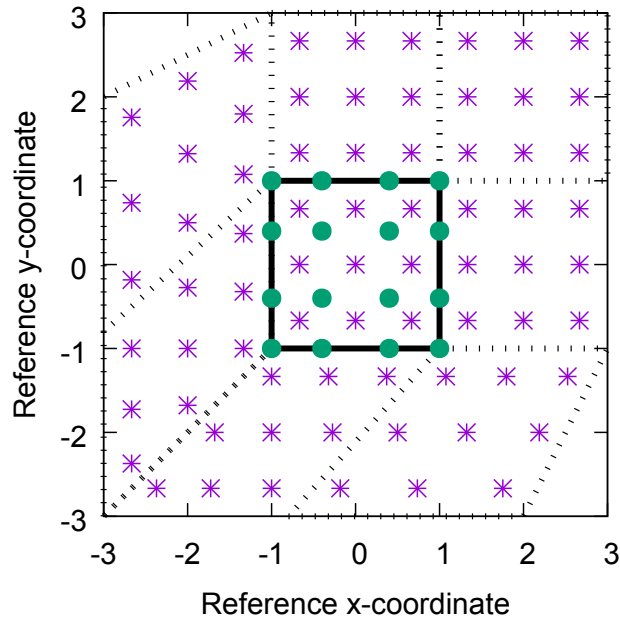
714 FIG. 10. Mean  $\omega$  at two model levels in the middle troposphere, in a Held-Suarez configuration outfitted with  
 715 real world topography. (Left) CAM-SE state on the GLL grid, *ne30np4*, (Middle) CAM-SE-CSLAM state on  
 716 the GLL grid, *ne30np4* and (Right) CAM-SE-CSLAM state on the physics grid, *ne30pg3*. The  $\omega$  fields are  
 717 computed from a 1200 day Held-Suarez simulation. The data are contoured according to a ‘cell fill’ approach,  
 718 in which the coupler grids (e.g., Figure 4) are used to delineate the vertices of the control volumes.



719 FIG. 11. Climatological total precipitation rate computed from the final 19 years of a pair of 20 year long  
 720 AMIP type simulations. (Left) CAM-SE, (middle) CAM-SE-CSLAM and (Right) their differences. The differ-  
 721 ence field is computed through bilinearly interpolating to a common latitude-longitude grid.



722 FIG. 12. Climatological total precipitation rate computed from the final 19 years of a suite of 20 year long  
 723 AMIP simulations, using CAM-SE (ne30np4), CAM-SE-CSLAM (ne30np3) and CAM-FV (f09). The top plot  
 724 is an observational product, the gridded GPCP climatological precipitation dataset.



725 FIG. 13. Schematic of the coordinate system in which the dimensionally split cubic Lagrange interpolation  
 726 is computed. The physics grid centers are marked with asterisks and the GLL points, we are interpolating to,  
 727 with solid filled circles. The element in which the GLL points are located is bounded by thick black lines and  
 728 located in the lower left corner of a panel. The stippled lines mark the boundaries of the remaining elements.  
 729 For simplicity we are using the normalized coordinate centered at the element on which the GLL points we are  
 730 interpolating to are located. Note that the coordinates for points on neighboring panels (using a different local  
 731 coordinate system) must be transformed to the coordinate system of the element in question.